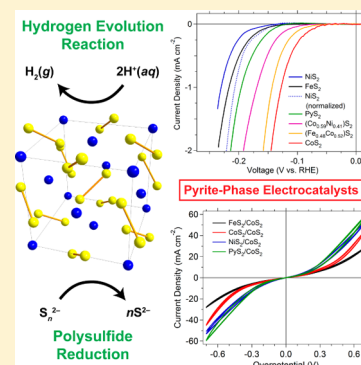


# Earth-Abundant Metal Pyrites ( $\text{FeS}_2$ , $\text{CoS}_2$ , $\text{NiS}_2$ , and Their Alloys) for Highly Efficient Hydrogen Evolution and Polysulfide Reduction Electrocatalysis

Matthew S. Faber, Mark A. Lukowski, Qi Ding, Nicholas S. Kaiser, and Song Jin\*

Department of Chemistry, University of Wisconsin—Madison, 1101 University Avenue, Madison, Wisconsin 53706, United States

**ABSTRACT:** Many materials have been explored as potential hydrogen evolution reaction (HER) electrocatalysts to generate clean hydrogen fuel via water electrolysis, but none so far compete with the highly efficient and stable (but cost prohibitive) noble metals. Similarly, noble metals often excel as electrocatalytic counter electrode materials in regenerative liquid-junction photoelectrochemical solar cells, such as quantum dot-sensitized solar cells (QDSSCs) that employ the sulfide/polysulfide redox electrolyte as the hole mediator. Here, we systematically investigate thin films of the earth-abundant pyrite-phase transition metal disulfides ( $\text{FeS}_2$ ,  $\text{CoS}_2$ ,  $\text{NiS}_2$ , and their alloys) as promising alternative electrocatalysts for both the HER and polysulfide reduction. Their electrocatalytic activity toward the HER is correlated to their composition and morphology. The emergent trends in their performance suggest that cobalt plays an important role in facilitating the HER, with  $\text{CoS}_2$  exhibiting highest overall performance. Additionally, we demonstrate the high activity of the transition metal pyrites toward polysulfide reduction and highlight the particularly high intrinsic activity of  $\text{NiS}_2$ , which could enable improved QDSSC performance. Furthermore, structural disorder introduced by alloying different transition metal pyrites could increase their areal density of active sites for catalysis, leading to enhanced performance.



## INTRODUCTION

The ability to efficiently and inexpensively generate hydrogen gas is essential to its proposed adoption as a sustainable, secure, and clean next-generation alternative energy carrier.<sup>1,2</sup> Various methods exist for producing hydrogen fuel,<sup>2</sup> but among these, water electrolysis (ideally driven by solar energy<sup>3–7</sup>) is most attractive. By electrocatalytically splitting water to give clean hydrogen fuel, no harmful byproducts are released; then, upon its consumption in the presence of air, only energy and water are produced.<sup>7</sup> Numerous inorganic materials have been investigated as potential hydrogen evolution reaction (HER) electrocatalysts,<sup>8</sup> but none so far match both the performance and stability of the noble metals, particularly platinum.<sup>9</sup> However, the scarcity and high cost of the noble metals inhibit the large-scale deployment of energy conversion technologies that utilize noble metal electrocatalysts.<sup>10</sup> By replacement of such precious metal electrocatalysts with high-performance substitutes composed entirely of earth-abundant elements,<sup>8,11–27</sup> the cost of electrochemical and photoelectrochemical hydrogen production could be considerably reduced.

Through substantial (and ongoing) research efforts, a number of earth-abundant materials have been identified as promising candidate HER electrocatalysts,<sup>8</sup> including  $\text{MoS}_2$ ,<sup>11–13</sup>  $\text{WS}_2$ ,<sup>14,15</sup> amorphous  $\text{MoS}_x$ ,<sup>16,17</sup> amorphous  $\text{Co-S}$ ,<sup>18</sup>  $\text{FeP}$ ,<sup>19</sup>  $\text{CoP}$ ,<sup>20</sup>  $\text{Ni}_2\text{P}$ ,<sup>21</sup>  $\text{Co}_0.6\text{Mo}_{1.4}\text{N}_2$ ,<sup>22</sup> and the Ni–Mo alloys,<sup>23,24</sup> among others. The cubic pyrite-phase transition metal dichalcogenides (with the general formula  $\text{MX}_2$ , where typically  $\text{M} = \text{Fe}$ ,  $\text{Co}$ , or  $\text{Ni}$  and  $\text{X} = \text{S}$  or  $\text{Se}$ ) have only recently emerged as efficient HER electrocatalysts,<sup>25–28</sup> despite the

suggestion over 20 years ago that they could catalyze the HER.<sup>29</sup> Within the family of transition metal pyrites, iron disulfide (iron pyrite,  $\text{FeS}_2$ ; “fool’s gold”), cobalt disulfide (cobalt pyrite,  $\text{CoS}_2$ ; catterite), and nickel disulfide (nickel pyrite,  $\text{NiS}_2$ ; vaesite) are common and well-studied minerals. Composed of first-row transition metals and rock-forming chalcogens, the transition metal pyrites are very abundant and inexpensive, making them particularly interesting as materials for energy conversion applications. For example, semiconducting  $\text{FeS}_2$  is presently under intense investigation as a potential earth-abundant solar light absorber.<sup>30–32</sup> The electrocatalytic properties of  $\text{FeS}_2$  have also been leveraged in dye-sensitized solar cells (DSSCs),<sup>33</sup> with nanorod arrays<sup>34</sup> and thin film electrodes prepared from a nanocrystal ink<sup>35</sup> enabling device performance competitive with that achieved using platinum counter electrodes. Similarly, both  $\text{FeS}_2$  and  $(\text{Fe},\text{Co})\text{S}_2$  alloys have been investigated as oxygen reduction reaction (ORR) electrocatalysts.<sup>36</sup> Both  $\text{FeS}_2$ <sup>37</sup> and  $\text{CoS}_2$ <sup>38</sup> are also promising electrode materials for lithium-ion batteries. Unlike the semiconducting pyrites,  $\text{CoS}_2$  is intrinsically a conductive metal, allowing it to be used directly as an electrode material. This has been demonstrated through the use of  $\text{CoS}_2$  thin films synthesized directly on glass as highly effective counter electrodes<sup>39</sup> in quantum dot-sensitized solar cells (QDSSCs)<sup>40,41</sup> that employ the sulfide/polysulfide redox

Received: June 24, 2014

Revised: August 26, 2014

Published: August 26, 2014

electrolyte as the hole-transporting medium. Graphene-based composite electrodes incorporating CoS<sub>2</sub> nanoparticles have also proven effective in reducing triiodide in DSSCs, exhibiting performance superior to that of platinum.<sup>42</sup> Recently, we employed nanostructuring strategies to further increase the activity of CoS<sub>2</sub> electrodes toward both polysulfide and triiodide reduction.<sup>26</sup> In this same work, thin films, microwires, and nanowires of CoS<sub>2</sub> prepared directly on conducting graphite supports were shown to exhibit excellent electrocatalytic activity toward the HER, with micro- and nanostructuring of the CoS<sub>2</sub> material synergistically enhancing both performance and stability.<sup>26</sup> As with FeS<sub>2</sub>, CoS<sub>2</sub> thin films and nanocrystals have also been investigated as ORR electrocatalysts,<sup>43–45</sup> further establishing its generality as a high-performance electrocatalyst. More recently, hollow spheres of CoS<sub>2</sub> and NiS<sub>2</sub> have been used in supercapacitors,<sup>46</sup> as have NiS<sub>2</sub> nanocubes.<sup>47</sup> These NiS<sub>2</sub> nanocubes were also demonstrated as efficient cocatalysts for the photocatalytic production of hydrogen.<sup>47</sup>

Here, we report the systematic investigation of the HER and polysulfide reduction electrocatalytic activity of various pyrite-phase transition metal disulfides, namely, FeS<sub>2</sub>, CoS<sub>2</sub>, NiS<sub>2</sub>, and their alloys. While each of the transition metal pyrites characterized here exhibits activity toward the HER, confirming the general electrocatalytic properties of the pyrites, we show that their performance (as measured by their ability to enable high catalytic current densities at low overpotentials) tends to increase with increasing cobalt content, with CoS<sub>2</sub> being superior, suggesting a special role for cobalt in facilitating the HER. We have similarly compared the polysulfide reduction activity of FeS<sub>2</sub>, NiS<sub>2</sub>, and an alloy thereof to that of CoS<sub>2</sub> and identified NiS<sub>2</sub> as possessing particularly high activity. Furthermore, we suggest that alloying may be an effective and general method for enhancing the electrocatalytic activity of the transition metal pyrites due to the introduction of structural disorder, which could increase their areal density of active sites for catalysis.

## ■ EXPERIMENTAL METHODS

All chemicals were purchased from Sigma-Aldrich and used without further purification, unless otherwise noted.

**Substrate Preparation.** Graphite disk substrates (6.0 mm diameter, <1 mm thick) were prepared by cutting and mechanically thinning slices of a graphite rod (Ultra Carbon Corp., Ultra “F” purity). Each slice of the graphite rod was abraded on both sides with SiC paper (Allied High Tech Products, Inc.; 320 grit) until a thin disk was obtained. Then one side of each graphite disk substrate was polished to a specular finish using 1200 grit SiC paper. The polished graphite disks were cleaned by sequential sonication (100 W) in neutral distilled water (Thermo Scientific, Barnstead Nanopure, 18.2 MΩ cm) for 10 min, then in aqua regia (3:1 HCl(aq)/HNO<sub>3</sub>(aq)) for 10 min, and again in fresh distilled water for 10 min to remove loose graphite dust and any metal impurities. Finally, the clean graphite disks were dried in a forced-air convection oven at 120 °C.

Borosilicate plate glass substrates (1.5 cm × 3.0 cm, 3.3 mm thick) were manually roughened on one side with SiC paper (320 grit) for several minutes and then ultrasonically cleaned (100 W) for 30 min in a detergent solution (Fisher Scientific, Versa-Clean, diluted 1:4 with deionized water). The glass substrates were then thoroughly rinsed with distilled water and ethanol and then blown dry under a stream of nitrogen. Finally,

the substrates were oxygen plasma cleaned (150 W rf, <200 mTorr, 1 sccm O<sub>2</sub>, 3 min) to remove any organic residues.

**Transition Metal Pyrite Thin Film Synthesis.** For the binary transition metal pyrite thin films on graphite, a 30 nm thick film of the corresponding high-purity metal (Kurt J. Lesker, ≥99.95%) was deposited onto the polished side of clean graphite disk substrates at a rate of 0.3 Å s<sup>−1</sup> by electron-beam evaporation. An alloy film consisting mostly of Ni and Fe was deposited by electron-beam evaporating 30 nm of permalloy (“Py”, HyMu 80 alloy: 80.00 Ni, 4.20 Mo, 0.50 Mn, 0.35 Si, 0.02 C, balance Fe) onto graphite disk substrates. To prepare iron/cobalt and nickel/cobalt pyrite alloy films, metal bilayers consisting of 15 nm of Fe over 15 nm of Co or 15 nm of Ni over 15 nm of Co, respectively, were sequentially electron-beam evaporated onto graphite disk substrates.

To convert the metal films to their corresponding disulfide, a simple thermal sulfidation procedure was used.<sup>26,39</sup> Briefly, the metalized substrates were loaded into the center of a fused silica tube on a home-built flow reactor equipped with both pressure and gas flow controllers. An alumina boat containing 2 g of S powder (99.5–100.5%) was placed in the tube at the farthest upstream position within the tube furnace (Lindberg/Blue M, TF55035A-1). The tube reactor was then purged of air and maintained at a slight positive pressure of 780 Torr under a steady flow of Ar carrier gas (99.999%) at 25 sccm. To initiate the conversion, the furnace temperature was ramped from room temperature to 500 °C at a rate of approximately 60 °C min<sup>−1</sup> and held for 1 h. Then the tube furnace was opened to allow natural cooling of the sample back to room temperature under Ar flow.

Electrodes for the fabrication of symmetrical electrochemical cells were prepared by electron-beam evaporating 50 nm of Fe, Co, Ni, or Py onto borosilicate glass substrates coated with a ~180 nm thick conducting CoS<sub>2</sub> film (prepared by thermally sulfidizing a 100 nm thick Co film<sup>39</sup>). Then these metal films were thermally sulfidized (using the same procedures described above) to yield FeS<sub>2</sub>, CoS<sub>2</sub>, NiS<sub>2</sub>, or permalloy pyrite (“PyS<sub>2</sub>”) thin films, respectively, electrically contacted directly by the underlying metallic CoS<sub>2</sub> film.

**Materials Characterization.** The as-synthesized pyrite films on graphite were characterized using a LEO SUPRA 55 VP field-emission scanning electron microscope operated at 5 kV and a Thermo Scientific DXR Raman microscope fitted with 532 nm excitation laser. X-ray photoelectron spectroscopy (XPS) was performed on the as-synthesized pyrite films on graphite using a Thermo Scientific K-Alpha XPS system with an Al Kα source. X-ray diffraction (XRD) patterns of the thicker pyrite films on glass were acquired on a Bruker D8 ADVANCE powder XRD using Cu Kα radiation. The XRD pattern background was fit to a cubic spline and subtracted using the Jade 5 software (Materials Data, Inc.).

**Electrochemical Characterization of Electrocatalytic Activity toward the HER.** All electrochemical characterizations of HER activity were performed in a three-electrode configuration and recorded using a Bio-Logic SP-200 potentiostat. Each measurement was performed in 0.5 M H<sub>2</sub>SO<sub>4</sub>(aq) electrolyte continuously purged with H<sub>2</sub>(g) (99.999%) using a saturated calomel reference electrode (SCE) (CH Instruments) and a graphite rod (National Carbon Co., AGKSP Spectroscopic Electrode) as the counter electrode. After characterization of pyrite film electrocatalytic activity toward the HER, the SCE was calibrated against the reversible hydrogen electrode (RHE) using platinum wire (Kurt J. Lesker,

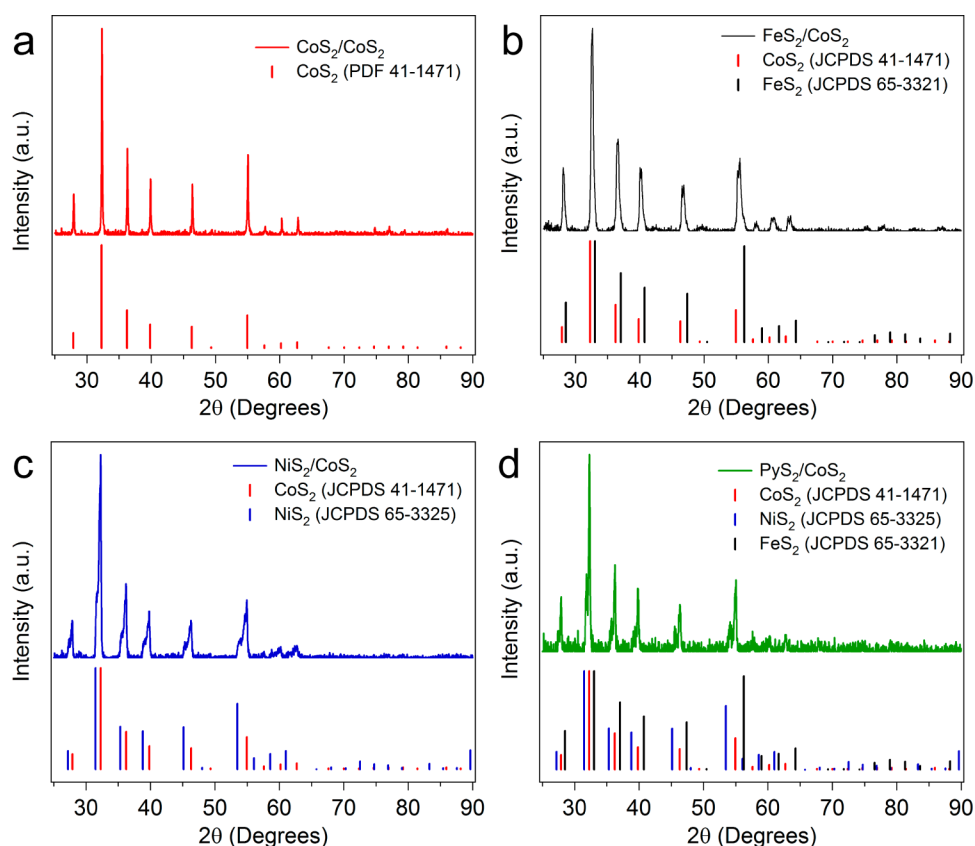


**Figure 1.** X-ray diffraction (XRD) patterns of as-prepared pyrite-phase (a)  $\text{CoS}_2$ , (b)  $\text{FeS}_2$ , (c)  $\text{NiS}_2$ , and (d)  $\text{PyS}_2$  electrocatalyst thin films over a  $\text{CoS}_2$  film on glass. In each panel, the standard diffraction patterns for  $\text{CoS}_2$  (JCPDS 41-1471),  $\text{FeS}_2$  (JCPDS 65-3321), and/or  $\text{NiS}_2$  (JCPDS 65-3325) appear below the experimental pattern.

99.99%; 0.50 mm diameter) as both the working and counter electrodes. The working electrode in each measurement was a pyrite thin film coated graphite disk sample mounted on a fluoropolymer (PCTFE) encased glassy carbon disk electrode using silver paint (Ted Pella, PELCO colloidal silver). Cyclic voltammograms (CVs) were recorded for each electrode from approximately +0.10 to  $-0.24$  V vs RHE at a scan rate of  $2 \text{ mV s}^{-1}$ , repeating this scan at least twice. Note that CV peaks that could be attributed to hydrogen underpotential deposition were not observed and the capacitive background currents were stable upon repeated cycling. Then electrochemical impedance spectroscopy (EIS) was performed in potentiostatic mode at  $-0.19$  V vs RHE, applying a sinusoidal voltage with an amplitude of 10 mV and scanning frequency from 200 kHz to 50 mHz. The EIS spectra were modeled using a simplified Randles equivalent circuit consisting of a resistor in series with a parallel arrangement of a constant phase element and a second resistor for the purpose of extracting the series resistance associated with each electrode. This series resistance ( $R$ ) represents all ohmic losses throughout the measurement setup, including the wiring, electrode, electrocatalyst, and solution resistances and enables their contributions to the measured overpotentials ( $IR$ ) to be subtracted.<sup>26</sup> All polarization curves were corrected for background current and  $IR$  losses, as described in detail previously,<sup>26</sup> and those presented here depict representative electrode behavior.

**Symmetrical Cell Fabrication and Electrochemical Characterization.** Symmetrical electrochemical cells were fabricated using freshly prepared pyrite film electrodes on glass and characterized in a two-electrode configuration using

procedures described elsewhere.<sup>26,39</sup> The sulfide/polysulfide electrolyte filled into the symmetrical cells consisted of 2 M  $\text{Na}_2\text{S} \cdot 9\text{H}_2\text{O}$  ( $\geq 99.99\%$ ) and 2 M S in aqueous solution. To ensure good electrical contact to the pyrite-phase electrocatalyst film on each electrode, the top pyrite film was lightly scratched using SiC paper and electrical contacts were applied directly to the underlying  $\text{CoS}_2$  film using silver paint.

## RESULTS AND DISCUSSION

**Pyrite Thin Film Synthesis and Structural Characterization.** The simplicity and generality of the thermal sulfidation procedure described here allow metallic thin films of iron, cobalt, nickel, and permalloy (which primarily consists of nickel and iron), as well as bilayer iron/cobalt and nickel/cobalt films, to be converted to their corresponding pyrite-phase disulfides using the same synthesis conditions (Experimental Methods). The resulting transition metal pyrite thin films adhere well to and uniformly cover the substrate surface (either graphite or glass). Two types of samples were prepared: thin pyrite films (less than 50 nm in thickness) on conductive graphite substrates for direct characterization of their HER electrocatalytic activity, and thick bilayer pyrite films on glass substrates for the assessment of their activity toward polysulfide reduction in symmetrical electrochemical cells (Experimental Methods). The thin pyrite-phase electrocatalyst films on graphite do not permit direct phase identification by X-ray diffraction (XRD) because of the low-signal pyrite diffraction peaks being overwhelmed by the reflections from the graphite support; however, the thicker films on glass clearly establish the formation of pyrite-phase products via thermal sulfidation



(Figure 1). In these diffraction patterns, the most intense peaks result from the underlying  $\text{CoS}_2$  film on glass (Figure 1a), which provides electrical contact to the uppermost pyrite-phase electrocatalyst layers. Peak broadening and/or the appearance additional peaks adjacent to the primary  $\text{CoS}_2$  peaks results from the presence of a  $\text{FeS}_2$ ,  $\text{NiS}_2$ , or  $\text{PyS}_2$  overlayer (Figure 1b–d). Because the pyrite phases are isostructural with one another and possess very similar lattice constants, XRD reaches its resolution limit and cannot effectively differentiate the pyrite-phase products, particularly in the case of  $\text{FeS}_2$  and  $\text{CoS}_2$  (Figure 1b).

Moreover, in the case of the permalloy and bilayer metal precursor films on graphite, pyrite-phase alloy thin films are obtained upon thermal sulfidation due to mixing of the metal species, further complicating their structural characterization by XRD. To effectively differentiate the different transition metal disulfide thin films on graphite, we instead used Raman spectroscopy both to verify the formation of pyrite-phase products and to qualitatively evaluate their composition and crystallinity. The Raman spectra of the thinner transition metal pyrite and pyrite alloy films on graphite are shown in Figure 2. The Raman spectra for the  $\text{FeS}_2$ ,  $\text{CoS}_2$ , and  $\text{NiS}_2$  thin films are in strong agreement with previous reports on the corresponding phase-pure pyrites,<sup>31,43</sup> with the sharp peaks associated with the distinct vibrational modes of the pyrite structure indicating long-range crystalline ordering. In contrast, the Raman peaks of the  $\text{PyS}_2$  thin film are very broad, possibly owing to the alloying

of multiple metal sulfides upon thermal sulfidation of permalloy; however, the primary peaks at 464 and 480  $\text{cm}^{-1}$  likely result from a composition consisting primarily of  $\text{NiS}_2$ , while the peak at 382  $\text{cm}^{-1}$  might indicate the presence of  $\text{FeS}_2$ . More importantly, the peaks are substantially broadened and reduced in intensity as compared to those of the binary pyrites, indicating greater structural disorder in the alloy film. Similarly, the Raman spectrum for the  $(\text{Fe},\text{Co})\text{S}_2$  thin film shows a broad peak centered around 371  $\text{cm}^{-1}$  which is likely the result of approximately equal contributions from the primary  $\text{CoS}_2$  peak at 393  $\text{cm}^{-1}$  and the most intense  $\text{FeS}_2$  peaks at 377 and 342  $\text{cm}^{-1}$ . Likewise, a very broad peak centered at 433  $\text{cm}^{-1}$  appears in the Raman spectrum of the  $(\text{Co},\text{Ni})\text{S}_2$  thin film owing to contributions from both  $\text{CoS}_2$  and  $\text{NiS}_2$  in a randomly mixed alloy. The increased full width at half maximum of this primary Raman feature suggests that the  $(\text{Co},\text{Ni})\text{S}_2$  films might possess even greater structural disorder than the  $(\text{Fe},\text{Co})\text{S}_2$  films. Had these pyrite-phase alloy thin films instead consisted of a bilayer (or mixture) of two distinct pyrite phases, we would have observed a simple superposition of the Raman spectra corresponding to the two phase-pure binary pyrites.

The Raman spectra confirm the formation of pyrite-phase products for the binary disulfides and strongly suggest the presence of pyrite-phase alloys for the other thin films, but they do not permit quantification of the surface composition of the alloys, which is particularly relevant in electrocatalysis. For the pyrite-phase alloy thin films on graphite, the exact ratio of transition metals at the film surface was determined using X-ray photoelectron spectroscopy (XPS) (Figure 3). Integration and comparison of the Fe 2p and Co 2p or Ni 2p and Co 2p signals revealed alloy compositions of  $(\text{Fe}_{0.48}\text{Co}_{0.52})\text{S}_2$  and  $(\text{Co}_{0.59}\text{Ni}_{0.41})\text{S}_2$ , respectively, for the thin films prepared by thermal sulfidation of the corresponding metal bilayers, confirming that there is substantial mixing of the metal films upon thermal sulfidation. Similarly, comparing the Ni 2p and Fe 2p peaks in the  $\text{PyS}_2$  XPS spectrum revealed an approximate surface composition of  $(\text{Fe}_{0.07}\text{Ni}_{0.93})\text{S}_2$  (not accounting for other minor species that may be present), consistent with the nickel-rich composition of permalloy.

Scanning electron microscopy (SEM) of the pyrite-phase thin films on graphite reveals that the as-sulfidized films generally consist of uniform nanocrystalline grains sintered together to cover the substrate surface (Figure 4), as previously reported.<sup>26,39</sup> The morphologies of the pyrite-phase thin films prepared on glass are very similar. While the polycrystalline pyrite-phase thin films all exhibit essentially the same appearance, there are important morphological differences that distinguish them from one another. In particular, the  $\text{NiS}_2$  grains, which are typically 80–200 nm in diameter and sintered into clusters to form a porous film, are substantially larger than those of  $\text{FeS}_2$  or  $\text{CoS}_2$ . Consistent with this observation, the other pyrite-phase films that contain a substantial amount of nickel, namely,  $\text{PyS}_2$  and  $(\text{Co}_{0.59}\text{Ni}_{0.41})\text{S}_2$ , also show the clustering of grains to give a more open film structure. Similarly, the  $(\text{Fe}_{0.48}\text{Co}_{0.52})\text{S}_2$  films feature both the compact morphology of the  $\text{CoS}_2$  films and the larger grain size of the  $\text{FeS}_2$  films.

**Electrocatalytic Performance of Pyrite Thin Films toward the HER.** By direct synthesis of the pyrite-phase electrocatalyst thin films on conducting graphite disk substrates, their electrocatalytic activity toward the HER can be easily assessed using standard electrochemical techniques. These characterizations were performed by interfacing the graphite-

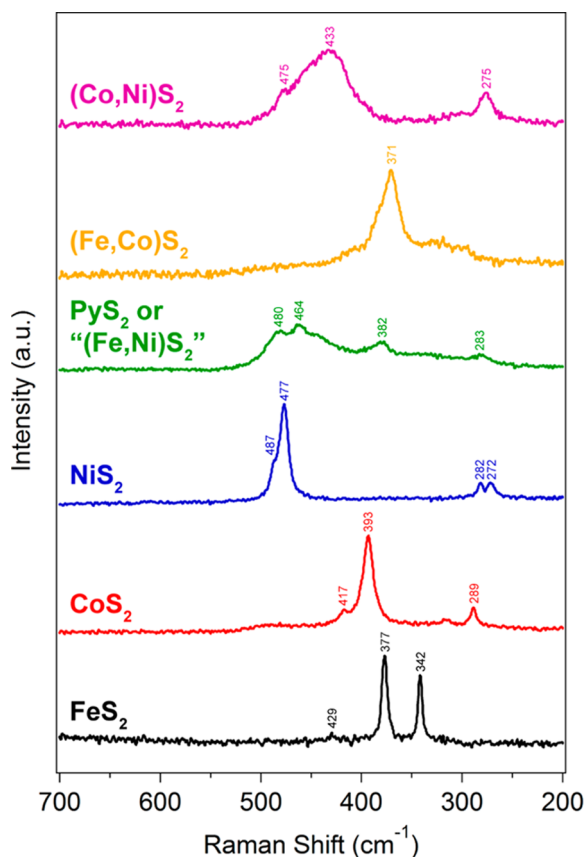


**Figure 2.** Raman spectra for iron pyrite ( $\text{FeS}_2$ , black trace), cobalt pyrite ( $\text{CoS}_2$ , red trace), nickel pyrite ( $\text{NiS}_2$ , blue trace), “permalloy pyrite” [ $\text{PyS}_2$  or  $(\text{Fe},\text{Ni})\text{S}_2$ ], green trace], iron/cobalt pyrite [ $(\text{Fe},\text{Co})\text{S}_2$ , orange trace], and cobalt/nickel pyrite [ $(\text{Co},\text{Ni})\text{S}_2$ , violet trace] thin films prepared on graphite disk substrates.

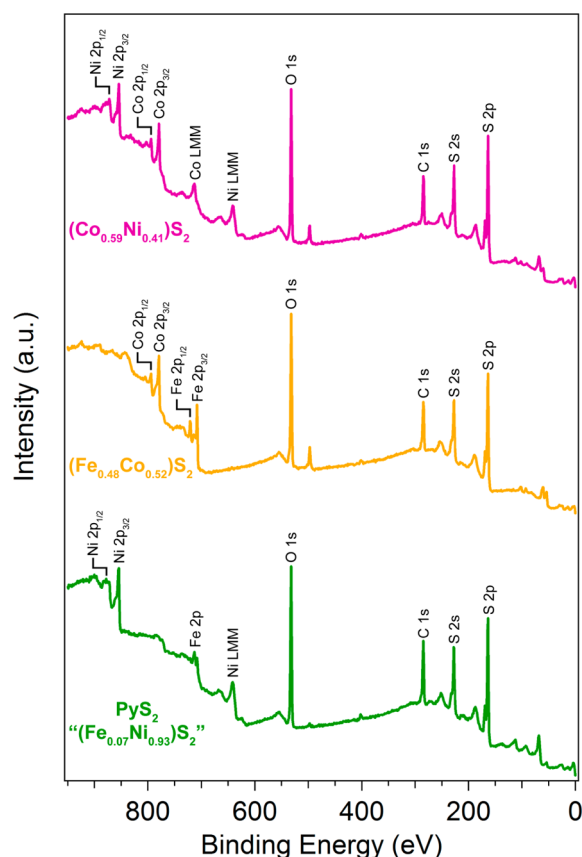


**Figure 3.** X-ray photoelectron spectroscopy (XPS) survey spectra of the pyrite-phase transition metal disulfide alloy thin films formed by thermally sulfidizing a permalloy film (bottom green trace), an iron/cobalt metal bilayer (middle orange trace), or a nickel/cobalt metal bilayer (top violet trace), which yield alloy compositions of “(Fe<sub>0.07</sub>Ni<sub>0.93</sub>)S<sub>2</sub>” (which is roughly commensurate with the composition of permalloy, not accounting for minor species), (Fe<sub>0.48</sub>Co<sub>0.52</sub>)S<sub>2</sub>, and (Co<sub>0.59</sub>Ni<sub>0.41</sub>)S<sub>2</sub>, respectively.

supported thin films with a glassy carbon disk electrode and measuring their voltammetric behavior in 0.5 M H<sub>2</sub>SO<sub>4</sub>(aq) electrolyte continuously purged with H<sub>2</sub>(g) in a three-electrode electrochemical measurement (Experimental Methods). Linear sweep voltammetric polarization curves showing the electrocatalytic current density ( $J$ ) produced by each of the pyrite-phase electrocatalyst thin film electrodes plotted against the applied potential appear in Figure 5a,b.

Figure 5a illustrates that all of the pyrite-phase thin films enable the electrocatalytic evolution of hydrogen gas, as indicated by the onset of current and the formation of bubbles at the electrode surface under cathodic bias. However, there is a marked difference in performance among the electrocatalysts, as highlighted in Figure 5b. If we measure the cathodic overpotential ( $\eta$ ) required for the different electrocatalysts to drive the HER at 1 mA cm<sup>-2</sup>, we notice that it steadily decreases in the order of NiS<sub>2</sub> ( $\eta$  = 230 mV) to FeS<sub>2</sub> ( $\eta$  = 217 mV) to PyS<sub>2</sub> ( $\eta$  = 196 mV) to (Co<sub>0.59</sub>Ni<sub>0.41</sub>)S<sub>2</sub> ( $\eta$  = 170 mV) to (Fe<sub>0.48</sub>Co<sub>0.52</sub>)S<sub>2</sub> ( $\eta$  = 143 mV) to CoS<sub>2</sub> ( $\eta$  = 128 mV), as summarized in Table 1. These overpotentials are roughly consistent with the apparent shifts in the onset of catalytic current for the different electrocatalysts, which compare favorably with those previously reported in the literature for both pyrite-phase HER electrocatalysts<sup>25–27</sup> and other earth-abundant HER electrocatalysts.<sup>11–24</sup> While the (Fe<sub>0.48</sub>Co<sub>0.52</sub>)S<sub>2</sub>

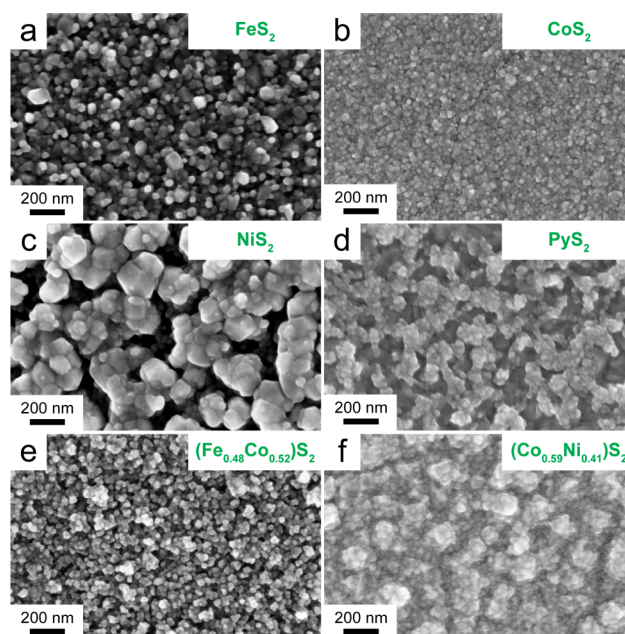


**Figure 4.** Scanning electron microscopy images of representative (a) FeS<sub>2</sub>, (b) CoS<sub>2</sub>, (c) NiS<sub>2</sub>, (d) PyS<sub>2</sub>, (e) (Fe<sub>0.48</sub>Co<sub>0.52</sub>)S<sub>2</sub>, and (f) (Co<sub>0.59</sub>Ni<sub>0.41</sub>)S<sub>2</sub> thin films prepared on graphite disk substrates depicting their small-grain polycrystalline texture.

and CoS<sub>2</sub> thin films are able to achieve  $J$  = −10 mA cm<sup>-2</sup> (at  $\eta$  = −196 mV and  $\eta$  = −192 mV, respectively), as shown in Figure 5a, the lower performing electrocatalysts do not reach this current density over the range of applied overpotentials. As we have shown previously, transition metal pyrite thin films on graphite tend to delaminate under the conditions of rapid hydrogen evolution that accompanies high current densities,<sup>26</sup> so we intentionally limited our characterizations to permit only modest current densities. The best electrocatalytic performance displayed by these pyrite thin films is comparable to what could be achieved for the metallic 1T-MoS<sub>2</sub> nanosheets<sup>11</sup> but lower than what was recently shown for the metallic 1T-WS<sub>2</sub> nanosheets.<sup>15</sup> However, unlike the metastable 1T-MX<sub>2</sub> nanosheets that need to be converted using lithium intercalation and exfoliation, the pyrite-phase electrocatalysts shown here are thermodynamically stable and, in the case of CoS<sub>2</sub>, intrinsically metallic.

Tafel analysis of the data presented in Figure 5a,b reveals that the Tafel slopes of all of the pyrite-phase electrocatalysts lie in the approximate range of 50–60 mV decade<sup>-1</sup> (Figure 5c and Table 1), consistent with previous reports.<sup>25–27</sup> Interestingly, the highest-performing CoS<sub>2</sub> film does not exhibit the highest intrinsic activity toward the HER, as indicated by its Tafel slope; it does, however, possess the highest geometric exchange current density ( $J_{0,\text{geometric}}$ ), which is characteristic of high electrocatalytic activity. The lowest-performing NiS<sub>2</sub> film actually shows a lower Tafel slope, consistent with a previous report,<sup>25</sup> suggesting that NiS<sub>2</sub> may in fact possess higher intrinsic activity toward the HER than CoS<sub>2</sub>. The  $J_{0,\text{geometric}}$  of NiS<sub>2</sub> is the lowest among those measured, which rationalizes its relatively poor performance among these pyrite-phase electrocatalysts. To better resolve these trends in performance and intrinsic activity, we must also consider the effective electrochemically active surface area of each pyrite-phase electrocatalyst film, since it is known to affect overall HER performance.<sup>26</sup> The double-layer capacitance ( $C_{\text{dl}}$ ) of each

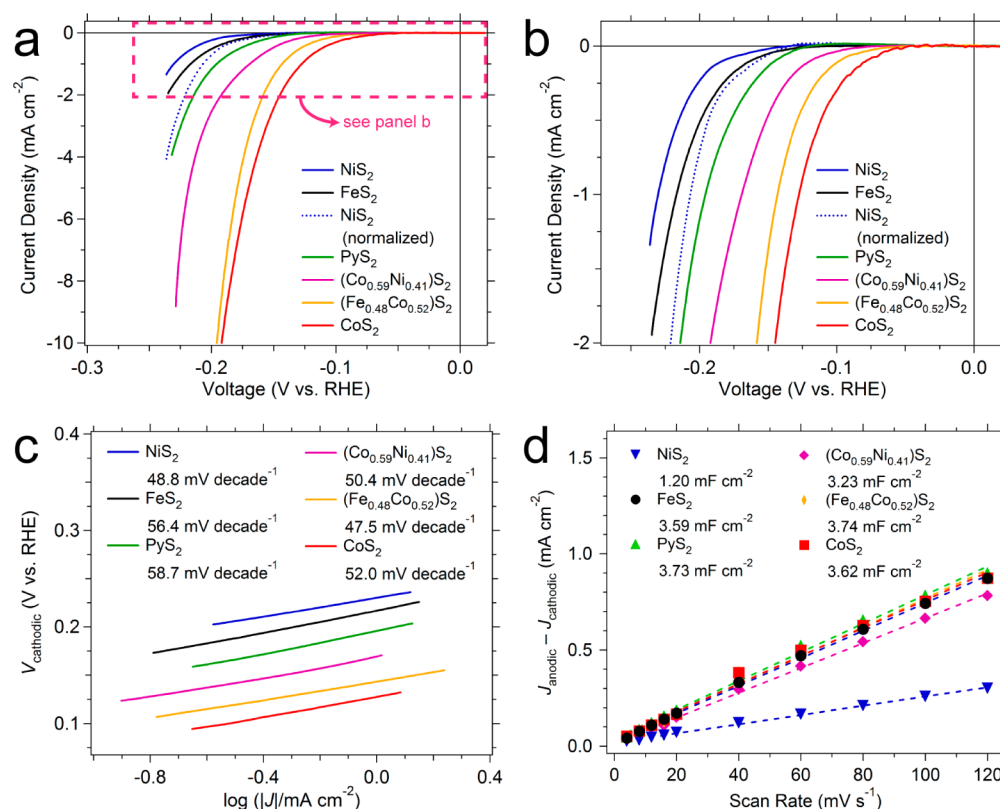


**Figure 5.** Electrochemical characterization of the catalytic activity of  $\text{FeS}_2$  (black traces and circle markers),  $\text{CoS}_2$  (red traces and square markers),  $\text{NiS}_2$  (blue traces and down-pointing triangles),  $\text{PyS}_2$  (green traces and up-pointing triangles),  $(\text{Fe}_{0.48}\text{Co}_{0.52})\text{S}_2$  (orange traces and thin diamond markers), and  $(\text{Co}_{0.59}\text{Ni}_{0.41})\text{S}_2$  (violet traces and diamond markers) thin films prepared on graphite disk substrates toward the HER. Polarization curves (corrected for background currents and IR losses) over (a) wider and (b) narrower ranges of current density comparing the performance of the pyrite-phase electrocatalyst thin films. The dashed trace presents the  $\text{NiS}_2$  data normalized by its relative surface area. (c) Tafel analysis of the data presented in panel a, with the specific Tafel slopes given in the figure legend. (d) Plot showing the method of extracting the double layer capacitance ( $C_{\text{dl}}$ ) for each electrode.

**Table 1. Summary of the Electrochemical Properties of the Different Pyrite-Phase Thin Film Electrocatalysts for the Hydrogen Evolution Reaction**

electrocatalyst	$\eta$ (mV vs RHE) for $J = -1 \text{ mA cm}^{-2}$	$\eta$ (mV vs RHE) for $J = -10 \text{ mA cm}^{-2}$	Tafel slope (mV decade <sup>-1</sup> )	$J_{0,\text{geometric}}$ ( $\mu\text{A cm}^{-2}$ )	$C_{\text{dl}}$ (mF cm <sup>-2</sup> )	relative surface area
$\text{FeS}_2$	-217	N/A	56.4	0.144	3.59	0.99
$\text{CoS}_2$	-128	-192	52.0	3.53	3.62	1.00
$\text{NiS}_2$	-230	N/A	48.8	0.0191	1.20	0.33
$\text{PyS}_2$ [ $(\text{Fe}_{0.07}\text{Ni}_{0.93})\text{S}_2$ ]	-196	N/A	58.7	0.0469	3.73	1.03
$(\text{Fe}_{0.48}\text{Co}_{0.52})\text{S}_2$	-143	-196	47.5	0.959	3.74	1.03
$(\text{Co}_{0.59}\text{Ni}_{0.41})\text{S}_2$	-170	N/A	50.4	0.0476	3.23	0.89

pyrite-phase electrocatalyst film, which is proportional to its effective surface area, was extracted using cyclic voltammetry (Experimental Methods), as shown in Figure 5d. All of the pyrite-phase electrocatalyst thin films exhibit similar values of  $C_{\text{dl}}$ , indicating comparable surface area, except  $\text{NiS}_2$ , for which the  $C_{\text{dl}}$  was approximately one-third that of the other electrocatalyst films. When these values of  $C_{\text{dl}}$  are compared against that of the  $\text{CoS}_2$  film (the highest performing electrocatalyst), we see that the relative surface area of the  $\text{NiS}_2$  film is indeed about one-third that of the other pyrite films (Table 1). This observation is consistent with their respective film morphologies as revealed by SEM (Figure 4), where the  $\text{NiS}_2$  film grains are substantially larger, likely resulting in a lower overall effective surface area. If the polarization data corresponding to the  $\text{NiS}_2$  film are normalized by the relative electrode surface area, the trace (Figure 5a,b, dashed blue line)

is shifted closer to that of the  $\text{PyS}_2$  electrode (green line), consistent with the nickel-rich composition of the  $\text{PyS}_2$  film. The results of these electrochemical characterizations are summarized in Table 1.

The electrochemical characterizations of the pyrite-phase electrocatalysts shown in Figure 5 indicate that their performance tends to increase with the introduction of cobalt, with  $\text{CoS}_2$  exhibiting the highest overall performance, suggesting that cobalt may energetically modify the active sites for catalysis (perhaps like a “promoter” species in the  $\text{MoS}_2$  system<sup>48</sup>) to facilitate the HER more effectively than iron or nickel. This is perhaps consistent with previous implications of the under-coordinated metal centers at low-index pyrite crystal faces, which resemble the active site of hydrogenase,<sup>49</sup> as being the active sites for HER electrocatalysis.<sup>25</sup> Interestingly, among the transition metal phosphide HER electrocatalysts,  $\text{CoP}^{20}$  also



exhibits superior performance as compared to  $\text{Ni}_2\text{P}^{21}$  and  $\text{FeP}^{19}$ . Similarly, the controlled introduction of cobalt to  $\delta$ - $\text{MoN}$  to form the  $\text{Co}_{0.6}\text{Mo}_{1.4}\text{N}_2$  phase substantially boosts its electrocatalytic activity toward the HER.<sup>22</sup> These examples echo our observations of improved performance for HER electrocatalysts that contain cobalt. Additionally, the improved performance of  $\text{PyS}_2$  and  $(\text{Ni}_{0.41}\text{Co}_{0.59})\text{S}_2$  (relative to that of  $\text{NiS}_2$ ) and  $(\text{Fe}_{0.48}\text{Co}_{0.52})\text{S}_2$  (relative to that of  $\text{FeS}_2$ ) suggests that alloying may also be an effective method for enhancing electrocatalytic activity. The structural disorder introduced through alloying could lead to a proliferation of active sites for catalysis, and the electronic interaction of multiple metal species may synergistically enhance intrinsic activity,<sup>8</sup> perhaps in the same way that amorphous  $\text{MoS}_x$  can exhibit intrinsic electrocatalytic activity toward the HER rivaling or even surpassing that of crystalline  $\text{MoS}_2$ .<sup>16,17</sup> Together, these conclusions suggest simple pathways toward improving the performance of the pyrite-phase transition metal disulfide electrocatalysts and have implications for other families of transition metal compound electrocatalysts.<sup>8</sup>

**Electrocatalytic Performance of Pyrite Thin Films toward Polysulfide Reduction.** Considering the high electrocatalytic activity of  $\text{CoS}_2$  toward polysulfide reduction<sup>26,39</sup> and the demonstrations here of the HER activity of other pyrite-phase transition metal disulfides, we probed the electrocatalytic activity of  $\text{FeS}_2$ ,  $\text{NiS}_2$ , and  $\text{PyS}_2$  thin films toward polysulfide reduction and compared their performance to that of  $\text{CoS}_2$ . The electrocatalyst thin films used in these characterizations were prepared on glass supports coated with a  $\sim 180$  nm thick film of conducting  $\text{CoS}_2$  (Experimental Methods). Cobalt pyrite was selected as the conductive electrocatalyst thin film support because of both its insensitivity to the thermal sulfidation conditions necessary to synthesize the  $\text{FeS}_2$ ,  $\text{NiS}_2$ , and  $\text{PyS}_2$  thin films as well as its known chemical compatibility with the sulfide/polysulfide electrolyte.

By use of these thin film electrodes, symmetrical electrochemical cells were assembled and filled with sulfide/polysulfide electrolyte (Experimental Methods). The performance of each electrocatalyst thin film was assessed in the symmetrical cell configuration using both cyclic voltammetry (CV) and electrochemical impedance spectroscopy (EIS) techniques (Experimental Methods). Remarkably, all of the pyrite-phase transition metal disulfide thin films show both good stability and high activity toward polysulfide reduction (Figure 6a). Moreover, both the  $\text{PyS}_2$  and, to a lesser extent,  $\text{NiS}_2$  films exhibit performance superior to that of  $\text{CoS}_2$ , as indicated by higher current densities across the full range of applied overpotentials. The  $\text{FeS}_2$  films, however, show performance inferior to that of the  $\text{CoS}_2$  films.

To understand the performance trends observed in the CV measurements, EIS was performed at the open circuit potential for each symmetrical cell device. The Nyquist plots shown in Figure 6b permit extraction of the series resistance ( $R_s$ ) and charge-transfer resistance ( $R_{ct}$ ) associated with each symmetrical cell device by fitting the experimental data to an equivalent circuit model (inset). The results of these fittings are displayed in Table 2. The  $R_s$  extracted for each electrode provides information about the electrical transport properties of each pyrite-phase electrocatalyst. Owing to its metallic conductivity,  $\text{CoS}_2$  shows the lowest  $R_s$ ; conversely, semi-conducting  $\text{FeS}_2$  shows the highest  $R_s$ , which supports the observation of lower current densities at high overpotentials in Figure 6a.  $\text{NiS}_2$  exhibits an intermediate  $R_s$  that is slightly higher

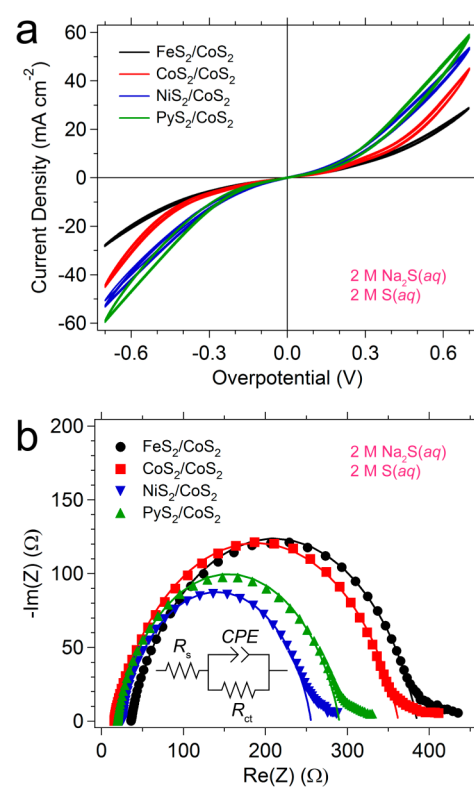


**Figure 6.** Electrochemical characterization of the pyrite-phase  $\text{FeS}_2$  (black traces and circle markers),  $\text{CoS}_2$  (red traces and square markers),  $\text{NiS}_2$  (blue traces and down-pointing triangles), and  $\text{PyS}_2$  (green traces and up-pointing triangles) electrocatalyst thin films prepared on  $\text{CoS}_2$ /glass electrodes toward polysulfide reduction in symmetrical electrochemical cells. (a) Cyclic voltammetry and (b) electrochemical impedance spectroscopy characterization of the symmetrical cells. The inset circuit diagram in panel b shows the equivalent circuit model used to fit the experimental data, with the results of these fittings shown as solid line traces.

**Table 2. Summary of the Electrochemical Properties of the Different Pyrite-Phase Thin Film Electrocatalysts for Polysulfide Reduction**

electrode	$R_s$ ( $\Omega$ )	$R_{ct}$ ( $\Omega \text{ cm}^2$ )
$\text{FeS}_2/\text{CoS}_2$	35.7	31.1
$\text{CoS}_2/\text{CoS}_2$	15.0	30.9
$\text{NiS}_2/\text{CoS}_2$	25.2	20.5
$\text{PyS}_2/\text{CoS}_2$	19.4	24.1

than that of  $\text{PyS}_2$ , which may have higher conductivity than  $\text{NiS}_2$  due to the minor presence of other metal sulfide species. More importantly, the values of  $R_{ct}$  provide information about the relative activity of the different pyrites toward polysulfide reduction. The  $\text{CoS}_2$  thin films show a value of  $R_{ct}$  similar to what has been previously reported,<sup>26,39</sup> and remarkably, the  $R_{ct}$  for  $\text{FeS}_2$  is quite comparable, indicating nearly equivalent levels of intrinsic activity toward polysulfide reduction. The  $R_{ct}$  of  $\text{NiS}_2$ , however, is the lowest, suggesting its superior activity toward polysulfide reduction. This observation is perhaps consistent with the low Tafel slope of  $\text{NiS}_2$  associated with HER electrocatalysis. This  $R_{ct}$  is still higher than that of the state-of-the-art reduced graphene oxide–cuprous sulfide ( $\text{RGO}-\text{Cu}_2\text{S}$ ) composite electrocatalyst that enables the highest QDSSC solar light-to-electricity conversion efficiencies.<sup>50</sup> The  $R_{ct}$  of  $\text{PyS}_2$  is higher than that of  $\text{NiS}_2$ , perhaps

because of iron alloying, but still lower than that of  $\text{CoS}_2$ . Coupled with its low  $R_s$ ,  $\text{PyS}_2$  enables the highest performance seen in the CV characterizations. These results indicate that, as in the case of HER electrocatalysis, multiple pyrite-phase transition metal disulfide compounds exhibit high activity toward polysulfide reduction. Furthermore,  $\text{NiS}_2$  possesses the highest intrinsic activity (even higher than that of  $\text{CoS}_2$ ), suggesting that its incorporation into QDSSC devices as the counter electrode electrocatalyst (perhaps as a composite with a conductive support, such as RGO, that facilitates electron transport) could enable improved solar light-to-electricity conversion efficiencies. Similarly, with the high activity of  $\text{FeS}_2$ ,  $\text{CoS}_2$ ,  $\text{NiS}_2$ , and other transition metal sulfide phases toward triiodide reduction already documented,<sup>26,34,35,42,46,47,51,52</sup> the trends observed here could potentially inform the development of improved pyrite-phase electrocatalysts for DSSC counter electrodes.

## SUMMARY AND PERSPECTIVES

In conclusion, we have demonstrated that both binary and alloyed pyrite-phase transition metal disulfide thin films can be prepared directly on graphite or glass substrates through the facile thermal sulfidation of metal precursor films and that these transition metal pyrite thin films are highly efficient HER and polysulfide reduction electrocatalysts. Current density–voltage characterizations of these pyrite-phase electrocatalyst thin films show the onset of  $\text{H}_2(\text{g})$  evolution at low overpotentials competitive with other earth-abundant electrocatalysts. The trends in their performance suggest that cobalt might play a special role in enhancing HER electrocatalytic performance. Additionally, Raman characterization of the alloy thin films confirms their increased structural disorder, which may contribute to their improved electrocatalytic performance. Furthermore, thin films of  $\text{FeS}_2$ ,  $\text{NiS}_2$ , and  $\text{PyS}_2$  were found to efficiently catalyze polysulfide reduction, with the intrinsic activity of  $\text{NiS}_2$  exceeding that of  $\text{CoS}_2$ . The general electrocatalytic activity of the pyrite-phase transition metal disulfides implies that a common feature might impart such activity. In addition to the effects of the transition metal cation on electrocatalytic activity reported here, the disulfide anions ( $\text{S}_2^{2-}$ ) present in all pyrite structures could be important for their high electrocatalytic activity toward the HER. Indeed, the disulfide-terminated edges of  $\text{MoS}_2$  and other layered transition metal dichalcogenides have been identified experimentally<sup>53</sup> and pursued in molecular mimics<sup>54,55</sup> as the active sites for HER electrocatalysis, again suggesting a catalytic role for disulfide. The abundance of disulfide-terminated surface sites in the pyrite crystal structure could contribute to the superb and general electrocatalytic activity of the pyrite-phase transition metal disulfides; however, additional mechanistic studies are required to establish such a relationship. Nevertheless, the trends observed in the electrocatalytic activity of these pyrite-phase thin films toward both the HER and polysulfide reduction suggest potential strategies for further boosting their performance in these and potentially other electrocatalytic and renewable energy applications.

## AUTHOR INFORMATION

### Corresponding Author

\*E-mail: jin@chem.wisc.edu.

### Notes

The authors declare no competing financial interest.

## ACKNOWLEDGMENTS

This research is supported by the U.S. Department of Energy, Office of Basic Energy Sciences, Division of Materials Sciences and Engineering, under Award DE-FG02-09ER46664. M.S.F. acknowledges support from the National Science Foundation Graduate Research Fellowship Program. S.J. thanks the Research Corporation for Science Advancement Scialog Award for Solar Energy Conversion and the University of Wisconsin—Madison H. I. Romnes Faculty Fellowship for support. XPS characterization was performed on instrumentation supported by the University of Wisconsin—Madison College of Engineering, Materials Research Science and Engineering Center (Grant NSF DMR-1121288), and Nano-scale Science and Engineering Center (Grant NSF DMR-0832760).

## REFERENCES

- (1) Lewis, N. S.; Nocera, D. G. Powering the Planet: Chemical Challenges in Solar Energy Utilization. *Proc. Natl. Acad. Sci. U.S.A.* **2006**, *103*, 15729–15735.
- (2) Turner, J. A. Sustainable Hydrogen Production. *Science* **2004**, *305*, 972–974.
- (3) Gray, H. B. Powering the Planet with Solar Fuel. *Nat. Chem.* **2009**, *1*, 7–7.
- (4) Chen, X. B.; Shen, S. H.; Guo, L. J.; Mao, S. S. Semiconductor-Based Photocatalytic Hydrogen Generation. *Chem. Rev.* **2010**, *110*, 6503–6570.
- (5) Walter, M. G.; Warren, E. L.; McKone, J. R.; Boettcher, S. W.; Mi, Q.; Santori, E. A.; Lewis, N. S. Solar Water Splitting Cells. *Chem. Rev.* **2010**, *110*, 6446–6473.
- (6) Nocera, D. G. The Artificial Leaf. *Acc. Chem. Res.* **2012**, *45*, 767–776.
- (7) Cook, T. R.; Dogutan, D. K.; Reece, S. Y.; Surendranath, Y.; Teets, T. S.; Nocera, D. G. Solar Energy Supply and Storage for the Legacy and Nonlegacy Worlds. *Chem. Rev.* **2010**, *110*, 6474–6502.
- (8) Faber, M. S.; Jin, S. Earth-Abundant Inorganic Electrocatalysts and Their Nanostructures for Energy Conversion Applications. *Energy Environ. Sci.* **2014**, DOI: 10.1039/C4EE01760A.
- (9) Nørskov, J. K.; Bligaard, T.; Logadottir, A.; Kitchin, J. R.; Chen, J. G.; Pandelov, S.; Stimming, U. Trends in the Exchange Current for Hydrogen Evolution. *J. Electrochem. Soc.* **2005**, *152*, J23–J26.
- (10) Vesborg, P. C. K.; Jaramillo, T. F. Addressing the Terawatt Challenge: Scalability in the Supply of Chemical Elements for Renewable Energy. *RSC Adv.* **2012**, *2*, 7933–7947.
- (11) Lukowski, M. A.; Daniel, A. S.; Meng, F.; Forticaux, A.; Li, L. S.; Jin, S. Enhanced Hydrogen Evolution Catalysis from Chemically Exfoliated Metallic  $\text{MoS}_2$  Nanosheets. *J. Am. Chem. Soc.* **2013**, *135*, 10274–10277.
- (12) Wang, H. T.; Lu, Z. Y.; Xu, S. C.; Kong, D. S.; Cha, J. J.; Zheng, G. Y.; Hsu, P.-C.; Yan, K.; Bradshaw, D.; Prinz, F. B.; et al. Electrochemical Tuning of Vertically Aligned  $\text{MoS}_2$  Nanofilms and Its Application in Improving Hydrogen Evolution Reaction. *Proc. Natl. Acad. Sci. U.S.A.* **2013**, *110*, 19701–19706.
- (13) Ding, Q.; Meng, F.; English, C. R.; Cabán-Acevedo, M.; Shearer, M. J.; Liang, D.; Daniel, A. S.; Hamers, R. J.; Jin, S. Efficient Photoelectrochemical Hydrogen Generation Using Heterostructures of Si and Chemically Exfoliated Metallic  $\text{MoS}_2$ . *J. Am. Chem. Soc.* **2014**, *136*, 8504–8507.
- (14) Voiry, D.; Yamaguchi, H.; Li, J. W.; Silva, R.; Alves, D. C. B.; Fujita, T.; Chen, M. W.; Asefa, T.; Shenoy, V. B.; Eda, G.; et al. Enhanced Catalytic Activity in Strained Chemically Exfoliated  $\text{WS}_2$  Nanosheets for Hydrogen Evolution. *Nat. Mater.* **2013**, *12*, 850–855.
- (15) Lukowski, M. A.; Daniel, A. S.; English, C. R.; Meng, F.; Forticaux, A.; Hamers, R. J.; Jin, S. Highly Active Hydrogen Evolution Catalysis from Metallic  $\text{WS}_2$  Nanosheets. *Energy Environ. Sci.* **2014**, *7*, 2608–2613.



- (16) Merki, D.; Fierro, S.; Vrubel, H.; Hu, X. L. Amorphous Molybdenum Sulfide Films as Catalysts for Electrochemical Hydrogen Production in Water. *Chem. Sci.* **2011**, *2*, 1262–1267.
- (17) Benck, J. D.; Chen, Z. B.; Kuritzky, L. Y.; Forman, A. J.; Jaramillo, T. F. Amorphous Molybdenum Sulfide Catalysts for Electrochemical Hydrogen Production: Insights into the Origin of their Catalytic Activity. *ACS Catal.* **2012**, *2*, 1916–1923.
- (18) Sun, Y. J.; Liu, C.; Grauer, D. C.; Yano, J.; Long, J. R.; Yang, P.; Chang, C. J. Electrodeposited Cobalt-Sulfide Catalyst for Electrochemical and Photoelectrochemical Hydrogen Generation from Water. *J. Am. Chem. Soc.* **2013**, *135*, 17699–17702.
- (19) Xu, Y.; Wu, R.; Zhang, J. F.; Shi, Y. M.; Zhang, B. Anion-Exchange Synthesis of Nanoporous FeP Nanosheets as Electrocatalysts for Hydrogen Evolution Reaction. *Chem. Commun.* **2013**, *49*, 6656–6658.
- (20) Popczun, E. J.; Read, C. G.; Roske, C. W.; Lewis, N. S.; Schaak, R. E. Highly Active Electrocatalysis of the Hydrogen Evolution Reaction by Cobalt Phosphide Nanoparticles. *Angew. Chem., Int. Ed.* **2014**, *53*, 5427–5430.
- (21) Popczun, E. J.; McKone, J. R.; Read, C. G.; Biacchi, A. J.; Wiltrout, A. M.; Lewis, N. S.; Schaak, R. E. Nanostructured Nickel Phosphide as an Electrocatalyst for the Hydrogen Evolution Reaction. *J. Am. Chem. Soc.* **2013**, *135*, 9267–9270.
- (22) Cao, B. F.; Veith, G. M.; Neuefeind, J. C.; Adzic, R. R.; Khalifah, P. G. Mixed Close-Packed Cobalt Molybdenum Nitrides as Non-Noble Metal Electrocatalysts for the Hydrogen Evolution Reaction. *J. Am. Chem. Soc.* **2013**, *135*, 19186–19192.
- (23) McKone, J. R.; Warren, E. L.; Bierman, M. J.; Boettcher, S. W.; Brunschwig, B. S.; Lewis, N. S.; Gray, H. B. Evaluation of Pt, Ni, and Ni–Mo Electrocatalysts for Hydrogen Evolution on Crystalline Si Electrodes. *Energy Environ. Sci.* **2011**, *4*, 3573–3583.
- (24) McKone, J. R.; Sadtler, B. F.; Werlang, C. A.; Lewis, N. S.; Gray, H. B. Ni–Mo Nanopowders for Efficient Electrochemical Hydrogen Evolution. *ACS Catal.* **2013**, *3*, 166–169.
- (25) Kong, D. S.; Cha, J. J.; Wang, H. T.; Lee, H. R.; Cui, Y. First-Row Transition Metal Dichalcogenide Catalysts for Hydrogen Evolution Reaction. *Energy Environ. Sci.* **2013**, *6*, 3553–3558.
- (26) Faber, M. S.; Dziedzic, R.; Lukowski, M. A.; Kaiser, N. S.; Ding, Q.; Jin, S. High-Performance Electrocatalysis Using Metallic Cobalt Pyrite (CoS<sub>2</sub>) Micro- and Nanostructures. *J. Am. Chem. Soc.* **2014**, *136*, 10053–10061.
- (27) Kong, D. S.; Wang, H. T.; Lu, Z. Y.; Cui, Y. CoSe<sub>2</sub> Nanoparticles Grown on Carbon Fiber Paper: An Efficient and Stable Electrocatalyst for Hydrogen Evolution Reaction. *J. Am. Chem. Soc.* **2014**, *136*, 4897–4900.
- (28) Ivanovskaya, A.; Singh, N.; Liu, R.-F.; Kreutzer, H.; Baltrusaitis, J.; Nguyen, T. V.; Metiu, H.; McFarland, E. Transition Metal Sulfide Hydrogen Evolution Catalysts for Hydrobromic Acid Electrolysis. *Langmuir* **2013**, *29*, 480–492.
- (29) Jaegermann, W.; Tributsch, H. Interfacial Properties of Semiconducting Transition Metal Chalcogenides. *Prog. Surf. Sci.* **1988**, *29*, 1–167.
- (30) Cabán-Acevedo, M.; Faber, M. S.; Tan, Y. Z.; Hamers, R. J.; Jin, S. Synthesis and Properties of Semiconducting Iron Pyrite (FeS<sub>2</sub>) Nanowires. *Nano Lett.* **2012**, *12*, 1977–1982.
- (31) Cabán-Acevedo, M.; Liang, D.; Chew, K. S.; DeGrave, J. P.; Kaiser, N. S.; Jin, S. Synthesis, Characterization, and Variable Range Hopping Transport of Pyrite (FeS<sub>2</sub>) Nanorods, Nanobelts, and Nanoplates. *ACS Nano* **2013**, *7*, 1731–1739.
- (32) Seefeld, S.; Limpinsel, M.; Liu, Y.; Farhi, N.; Weber, A.; Zhang, Y. N.; Berry, N.; Kwon, Y. J.; Perkins, C. L.; Hemminger, J. C.; et al. Iron Pyrite Thin Films Synthesized from an Fe(acac)<sub>3</sub> Ink. *J. Am. Chem. Soc.* **2013**, *135*, 4412–4424.
- (33) Hagfeldt, A.; Boschloo, G.; Sun, L. C.; Kloo, L.; Pettersson, H. Dye-Sensitized Solar Cells. *Chem. Rev.* **2010**, *110*, 6595–6663.
- (34) Huang, Q.-H.; Ling, T.; Qiao, S.-Z.; Du, X.-W. Pyrite Nanorod Arrays as an Efficient Counter Electrode for Dye-Sensitized Solar Cells. *J. Mater. Chem. A* **2013**, *1*, 11828–11833.
- (35) Wang, Y.-C.; Wang, D.-Y.; Jiang, Y.-T.; Chen, H.-A.; Chen, C.-C.; Ho, K.-C.; Chou, H.-L.; Chen, C.-W. FeS<sub>2</sub> Nanocrystal Ink as a Catalytic Electrode for Dye-Sensitized Solar Cells. *Angew. Chem., Int. Ed.* **2013**, *52*, 6694–6698.
- (36) Susac, D.; Zhu, L.; Teo, M.; Sode, A.; Wong, K. C.; Wong, P. C.; Parsons, R. R.; Bizzotto, D.; Mitchell, K. A. R.; Campbell, S. A. Characterization of FeS<sub>2</sub>-Based Thin Films as Model Catalysts for the Oxygen Reduction Reaction. *J. Phys. Chem. C* **2007**, *111*, 18715–18723.
- (37) Li, L. S.; Cabán-Acevedo, M.; Girard, S. N.; Jin, S. High-Purity Iron Pyrite (FeS<sub>2</sub>) Nanowires as High-Capacity Nanostructured Cathodes for Lithium-Ion Batteries. *Nanoscale* **2014**, *6*, 2112–2118.
- (38) Wang, Q. H.; Jiao, L. F.; Han, Y.; Du, H. M.; Peng, W. X.; Huan, Q. N.; Song, D. W.; Si, Y. C.; Wang, Y. J.; Yuan, H. T. CoS<sub>2</sub> Hollow Spheres: Fabrication and Their Application in Lithium-Ion Batteries. *J. Phys. Chem. C* **2011**, *115*, 8300–8304.
- (39) Faber, M. S.; Park, K.; Cabán-Acevedo, M.; Santra, P. K.; Jin, S. Earth-Abundant Cobalt Pyrite (CoS<sub>2</sub>) Thin Film on Glass as a Robust, High-Performance Counter Electrode for Quantum Dot-Sensitized Solar Cells. *J. Phys. Chem. Lett.* **2013**, *4*, 1843–1849.
- (40) Selinsky, R. S.; Ding, Q.; Faber, M. S.; Wright, J. C.; Jin, S. Quantum Dot Nanoscale Heterostructures for Solar Energy Conversion. *Chem. Soc. Rev.* **2013**, *42*, 2963–2985.
- (41) Kamat, P. V. Quantum Dot Solar Cells. The Next Big Thing in Photovoltaics. *J. Phys. Chem. Lett.* **2013**, *4*, 908–918.
- (42) Duan, X. L.; Gao, Z. Y.; Chang, J. L.; Wu, D. P.; Ma, P. F.; He, J. J.; Xu, F.; Gao, S. Y.; Jiang, K. CoS<sub>2</sub>–Graphene Composite as Efficient Catalytic Counter Electrode for Dye-Sensitized Solar Cell. *Electrochim. Acta* **2013**, *114*, 173–179.
- (43) Zhu, L.; Susac, D.; Teo, M.; Wong, K. C.; Wong, P. C.; Parsons, R. R.; Bizzotto, D.; Mitchell, K. A. R.; Campbell, S. A. Investigation of CoS<sub>2</sub>-Based Thin Films as Model Catalysts for the Oxygen Reduction Reaction. *J. Catal.* **2008**, *258*, 235–242.
- (44) Jirkovský, J. S.; Björling, A.; Ahlberg, E. Reduction of Oxygen on Dispersed Nanocrystalline CoS<sub>2</sub>. *J. Phys. Chem. C* **2012**, *116*, 24436–24444.
- (45) Zhao, C.; Li, D. Q.; Feng, Y. J. Size-Controlled Hydrothermal Synthesis and High Electrocatalytic Performance of CoS<sub>2</sub> Nanocatalysts as Non-Precious Metal Cathode Materials for Fuel Cells. *J. Mater. Chem. A* **2013**, *1*, 5741–5746.
- (46) Peng, S. J.; Li, L. L.; Tan, H. T.; Cai, R.; Shi, W. H.; Li, C. C.; Mhaisalkar, S. G.; Srinivasan, M.; Ramakrishna, S.; Yan, Q. Y. MS<sub>2</sub> (M = Co and Ni) Hollow Spheres with Tunable Interiors for High-Performance Supercapacitors and Photovoltaics. *Adv. Funct. Mater.* **2014**, *24*, 2155–2162.
- (47) Pang, H.; Wei, C. Z.; Li, X. X.; Li, G. C.; Ma, Y. H.; Li, S. J.; Chen, J.; Zhang, J. S. Microwave-Assisted Synthesis of NiS<sub>2</sub> Nanostructures for Supercapacitors and Cocatalytic Enhancing Photocatalytic H<sub>2</sub> Production. *Sci. Rep.* **2014**, DOI: 10.1038/srep03577.
- (48) Bonde, J.; Moses, P. G.; Jaramillo, T. F.; Nørskov, J. K.; Chorkendorff, I. Hydrogen Evolution on Nano-Particulate Transition Metal Sulfides. *Faraday Discuss.* **2008**, *140*, 219–231.
- (49) Du, P. W.; Eisenberg, R. Catalysts Made of Earth-Abundant Elements (Co, Ni, Fe) for Water Splitting: Recent Progress and Future Challenges. *Energy Environ. Sci.* **2012**, *5*, 6012–6021.
- (50) Radich, J. G.; Dwyer, R.; Kamat, P. V. Cu<sub>2</sub>S Reduced Graphene Oxide Composite for High-Efficiency Quantum Dot Solar Cells. Overcoming the Redox Limitations of S<sup>2-</sup>/S<sub>n</sub><sup>2-</sup> at the Counter Electrode. *J. Phys. Chem. Lett.* **2011**, *2*, 2453–2460.
- (51) Chang, S.-H.; Lu, M.-D.; Tung, Y.-L.; Tuan, H.-Y. Gram-Scale Synthesis of Catalytic Co<sub>9</sub>S<sub>8</sub> Nanocrystal Ink as a Cathode Material for Spray-Deposited, Large-Area Dye-Sensitized Solar Cells. *ACS Nano* **2013**, *7*, 9443–9451.
- (52) Wang, M. K.; Anghel, A. M.; Marsan, B.; Ha, N.-L. C.; Pootrakulchote, N.; Zakeeruddin, S. M.; Grätzel, M. CoS Supersedes Pt as Efficient Electrocatalyst for Triiodide Reduction in Dye-Sensitized Solar Cells. *J. Am. Chem. Soc.* **2009**, *131*, 15976–15977.

(53) Jaramillo, T. F.; Jørgensen, K. P.; Bonde, J.; Nielsen, J. H.; Horch, S.; Chorkendorff, I. Identification of Active Edge Sites for Electrochemical H<sub>2</sub> Evolution from MoS<sub>2</sub> Nanocatalysts. *Science* **2007**, *317*, 100–102.

(54) Karunadasa, H. I.; Montalvo, E.; Sun, Y. J.; Majda, M.; Long, J. R.; Chang, C. J. A Molecular MoS<sub>2</sub> Edge Site Mimic for Catalytic Hydrogen Generation. *Science* **2012**, *335*, 698–702.

(55) Kibsgaard, J.; Jaramillo, T. F.; Besenbacher, F. Building an Appropriate Active-Site Motif into a Hydrogen-Evolution Catalyst with Thiomolybdate [Mo<sub>3</sub>S<sub>13</sub>]<sup>2−</sup> Clusters. *Nat. Chem.* **2014**, *6*, 248–253.